Journal of Materials Chemistry C

Accepted Manuscript

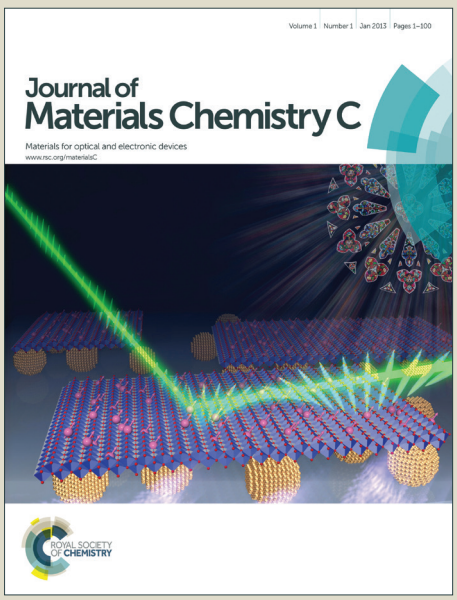

ROYAL SOCIETY OF CHEMISTRY

www.rsc.org/materialsC

Journal of Materials Chemistry C RSCPublishing

ARTICLE

Coupling of plasmon and 3D antireflection quasi-photonic crystal structure for enhancement infrared absorption

Cite this: DOI: 10.1039/x0xx00000x

Received ooth January 2012,
Accepted ooth January 2012

DOI: 10.1039/x0xx00000x

www.rsc.org/

Junlong Tian, Wang Zhang,* Qinglei Liu, Jiajun Gu, Tao Deng and Di Zhang*

In this study, the carbon-matrix Ag wing with a hierarchical sub-micron antireflection quasi-photonic crystal structure (HSAS) was fabricated by a simple and promising method. This method combines chemosynthesis with biomimetic techniques, without the requirement of expensive equipment and energy intensive processes. Here, the *Troides helena* (Linnaeus) (*T.helena*) forewing (T_FW) was chosen as the biomimetic template. The carbon-matrix Ag butterfly wing (Ag@C_T_FW) achieves a drastically enhanced infrared absorption over a broad spectral range, especially, over the near infrared region. Here we report methods to enhance and modify the plasmonic resonances in such structures by strongly coupling plasmonic resonances to HSAS. Using the finite difference time domain (FDTD) method, the absorption spectra and the distribution of the energy density near the Ag NPs surface were simulated. Based on the experiment and simulation results, these finding demonstrates that the enhanced infrared absorption over a broad spectral range is due to the mechanism that the plasmon and the coherent coupling between adjacent resonant systems integrate with the HSAS.

Introduction

The resonant excitation of plasmons in metallic nanostructures can provide large electromagnetic enhancements on the surfaces of metals.[1, 2] Such field enhancement can be exploited for wide-ranging applications in the sensing,[3-5] enhancing spectral signals,[6] probing catalytic reactions,[7] photothermal therapy,[6, 8, 9] surface enhanced raman scattering,[10-13] surface enhanced visible spectra absorption[14-17] and surface enhanced infrared (IR) absorption[18-21]. However, compared with other applications, the application of surface enhanced IR absorption attracted fewer attentions due to the limitations in designing and fabricating nanostructures with reproducible tunable plasmon resonances across a broadband IR region.[22-25] The maximum electromagnetic enhancement in a plasmonic nanostructure occurs for resonant excitations of the plasmons, which are typically found in the visible light and ultraviolet light regions. However, the plasmon resonances are tunability because the plasmon resonances of metallic nanoparticles are strongly dependent on structure and composition.[26] And then, the plasmon resonance is tuned over a wide spectral region, particularly in the near infrared (NIR) region.[27, 28] Furthermore, the plasmon resonances can also be tuned by modifying the plasmonic interactions that include the plasmonic interactions among the adjacent resonant systems[22] and the plasmonic interactions between the plasmonic components and structure.[29] As yet, many works integrate plasmonic components into corresponding functional structure to create, enhance or tailor the properties of materials.[29-32] However, self-assembly of these so-called plasmon resonance nanoparticles (NPs) into thin films and bulk materials on a macro-scale, particulary with related functional sub-micron structures, is difficult using conventional technologies, such as spontaneous epitaxial nucleation, chemosynthesis, growth of a second and third component onto seed NPs and the convective assisted capillary force assembly method.[30, 33-36]

In order to integrate plasmonic components into a 3D sub-micron antireflection quasi-photonic crystal structure (HSAS) to enhance and modify the plasmonic resonances in such structures, in this paper, the carbon-matrix Ag wing (Ag@C_T_FW) with HSAS was fabricated by a simple, cost-effective and promising method. This method combines chemosynthesis and biomimetic techniques using the *T. helena* (Linnaeus) forewing (T_FW) as the biomimetic template. Because the black forewing of the *T. helena* exhibits strong absorption of visible light, through the coupling effect of melanin/chitin composite and the HSAS of its scales.[37, 38] In order to illustrate the mechanism that the plasmon and the coherent coupling between adjacent resonant systems integrate with the HSAS to enhance IR absorption over a broad spectral

range, we systematically studied the optical absorption properties and the distribution of the energy density of the Ag nanospheres array, T_FW, Ag wing (Ag_T_FW) and Ag@C_T_FW by experiment and the finite difference time domain (FDTD) simulation analysis. Based on the experimental and simulation analysis, these results demonstrated that the Ag@C_T_FW and Ag_T_FW possessed enhancement broadband light absorption, specifically in the IR regions. The reason is that Ag@C_T_FW and Ag_T_FW integrated plasmon into HSAS. Consequently, the work successfully provides a new route that couple plasmonic resonances to HSAS to enhance broadband IR absorption and utilize the solar energy in IR range at lower cost. And appear to be useful in applications of plasmon for optoelectronics, photovoltaics, photothermal and related technologies.

Experimental section and simulation

Materials

T. helena butterflies were obtained from Shanghai Natural Wild-Insect Kingdom Co., Ltd. Absolute ethanol (EA, 97%) was purchased from Changshu Yangyuan Chemical Co., Ltd. Nitric acid (NA, 67%), ethylenediamine (ED, 99%), silver nitrate ($AgNO_3$), ammonium hydroxide ($NH_3 \cdot H_2O$) and potassium sodium tartrate were purchased from Sinopharm Chemical Reagent Co., Ltd. All of these compounds are analytically pure and were used as received without further purification.

Characterization

Characterization using scanning electron microscope (SEM) was performed on a 20-kV field emission SEM (FESEM) instrument (Quanta 250, FEI, Hillsboro, OR, USA). X-ray diffraction measurements were conducted using a Rigaku D/max-2550 instrument equipped with a Cu-Kα radiation source (Rigaku Corp., Tokyo, Japan). Transmission electron microscope (TEM), high resolution transmission electron microscope (HRTEM) and selected area electron diffraction (SAED) measurements were performed on a JEM-2100F transmission electron microscope (JEOL, Peabody, MA, USA) operated an acceleration voltage of 200 kV. The absorption over the wavelength range of 300-2500 nm was measured using a Lambda 750 UV-VIS-NIR spectrophotometer (PerkinElmer, Waltham, MA, USA). The samples were mounted for UV-VIS-NIR spectroscopy using the clip directly located behind the integrating sphere without any substrates. The IR absorption over the wavelength range of 2.5-15 μm was measured by Nicolet 6700 (Thermo Fisher Scientific) Fourier Transform infrared spectroscopy (FTIR).

Fabrication of Ag@C_T_FW

The procedure of fabricating the Ag@C_T_FW includes two steps (Fig. 1). Firstly, to prepare the Ag butterfly wing (Ag _T_FW), T_FW were first immersed in dilute 8 vol% nitric acid for 2 h, and then washed in deionized water. The wings were then immersed into ethanol solution of ethanediamine (25 vol%) for 6 h to obtained the aminated T_FW, and then washed with ethanol and deionized water. In succession, the aminated T_FW was immersed into the electroless plating solutions and followed by standard electroless deposition of Ag NPs onto the T_FW. The deposition was performed over a period of 15 min, and then rinsed them with deionized water and drying in vacuum drying oven at 25 ˚C in order to prevent these Ag wings from being oxidized. The electroless plating solution is composed of silver nitrate (1 g), ammonium hydroxide (2 mL), potassium sodium tartrate (5 g) and deionized water (100 mL).[12] Compared with the previous work for versatile fabrication of metallic butterfly wing,[12] to eliminate the interference from the plasmon resonant of Au NPs, we did not form the Au nanoparticle (NP) seeds on the aminated bio-surface to fabricate the Au-NP-functionalized butterfly wings. All of immersions were placed in thermostatic waterbath at 25 ˚C. Secondly, carbonization of the Ag_T_FW using a vacuum tube furnace heated to 450 ˚C at 3 ˚C·min^{-1} was performed for 2 h under vacuum conditions to produce the final Ag@C_T_FW.

Fig. 1. Schematic representation of the procedure of fabricating the Ag@C_T_FW by electroless deposition and carbonization.

Finite Difference Time Domain Method

The detailed FDTD model of the Ag nanospheres array (Ag), added the Ag nanospheres array to the surface of chitin sheet (Ag_chitin), T_FW and Ag_T_FW are shown in Fig. 2. All simulations are performed under normal incident light with the plane wave light source with laid above the ridges at a distance of 500 nm and the red arrow represents the incidence direction of the light. The reflection (R) monitor is located at behind of the light source at a distance of 500 nm. The transmission (T) monitor is located 100 nm beneath the model. (Fig. 2(d)) The absorption is deduced from A=1–T–R. The boundary condition in y directions is periodic (periodic boundary condition, PBC), and in x direction is absorbing (perfectly matched layer, PML). The span of z direction is zero. Here, in our simulation, the complex permittivity index of the Ag and chitin are provided by the material database of the Optiwave and the reported results,[38] respectively. In order to be consistent with the diameter of the Ag NPs deposited on the surface of the HSAS of Ag@C_T_FW as shown in Fig. 4(c) and (d), the diameter of the Ag nanosphere is set as 20 nm. The dimensions of d1-d8 and θ were offered in the Table 1, which are based on careful observation and statistical analysis of several SEM and TEM images of T_FW (Fig. 2(e)-(h)). The mesh size was chosen to obtain a good tradeoff between the computer memory required and the simulation time, while ensuring convergence of the results. A convergence test was carefully performed.

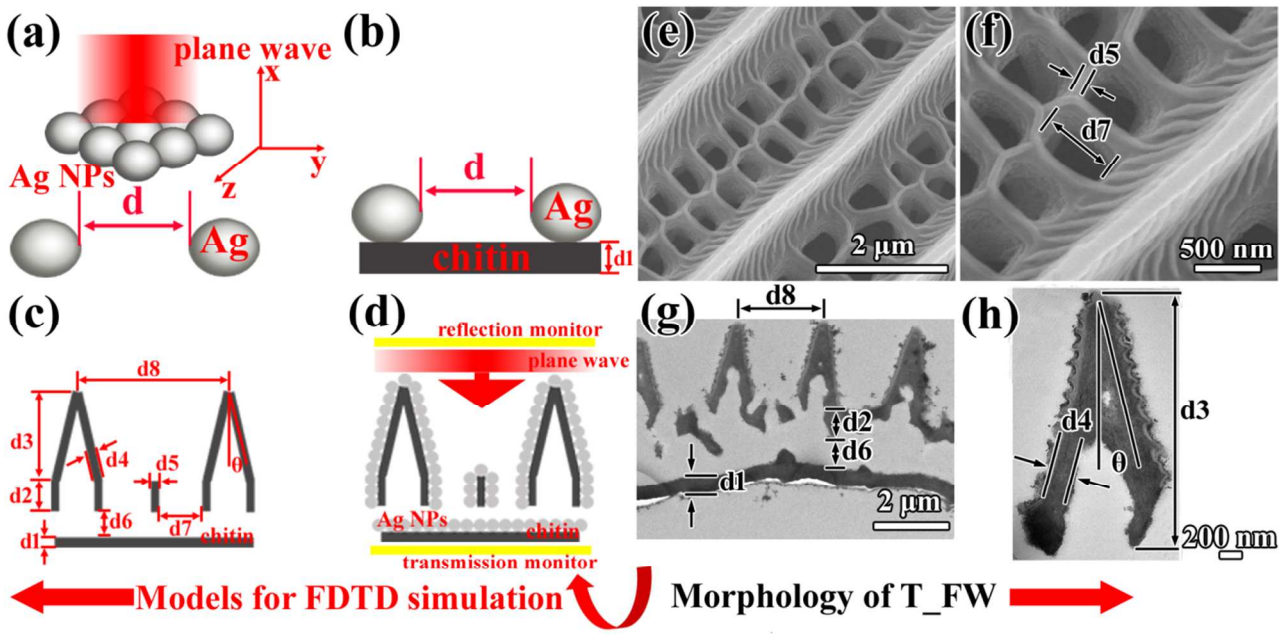

Fig. 2. Models for FDTD simulation of (a) Ag nanospheres array (Ag), (b) added the Ag nanospheres array to the surface of chitin (Ag_chitin), (c) T_FW and (d) added the Ag nanospheres array to the surface of T_FW (Ag_T_FW). (e) and (f) SEM images of T_EM. (g) and (h) TEM images of T_EM.

Table 1. The dimensions of d1-d8 and θ

	d1(μm)	d2(μm)	d3(μm)	d4(μm)	d5(μm)	d6(μm)	d7(μm)	d8(μm)	θ(°)
Value	0.460	0.900	3.270	0.200	0.200	1.010	0.530	2.870	13.0
Variance	0.003	0.016	0.046	0.001	0.001	0.004	0.003	0.002	--

Results and discussion

The depositing of Ag NPs onto the butterfly wing was examined by XRD measurements. As revealed by the XRD results in Fig. 3, the diffraction peaks of Ag_T_FW and Ag@C_T_FW with 2θ values of 38º, 44º, 64º, 77º and 81º are assigned to the (111), (200), (220), (311) and (222) planes of cubic phase Ag, respectively (JCPDS card no. 04-0783, silver-3C, syn). The well-defined peaks in the XRD pattern indicate the formation of cubic phase Ag nanoparticles with high crystallinity. In Fig. 3(b), a broad peak located near 2θ=20° is corresponding to the amorphous carbon. These results confirm the successful fabrication of Ag_T_FW and Ag@C_T_FW.

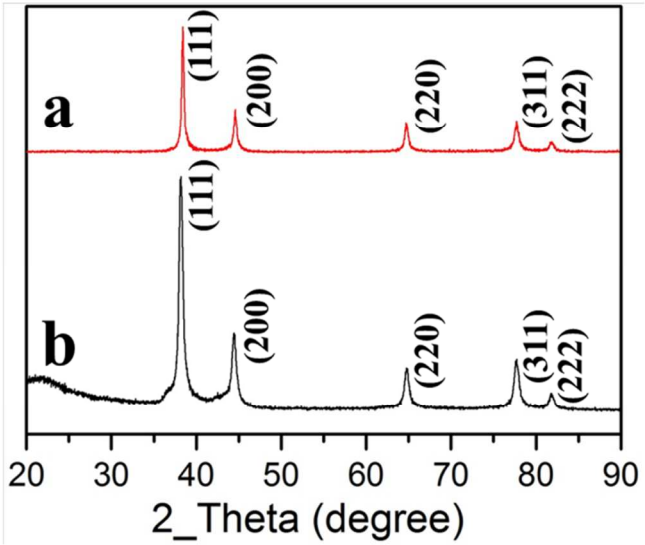

Fig. 3. XRD results of (a) Ag_T_FW, (b) Ag@C_T_FW

The morphologies of the Ag butterfly wings and the carbon-matrix Ag butterfly wings were characterized using FESEM and TEM (Fig. 4). As showed in Fig. 4(a), the Ag nanoparticles were deposited and agglomerated into thin metal film on the ridges and ribs of the T_FW, when the electroless plating time lasted for 15 min (Ag_T_FW). Moreover, the parallel periodic

triangular roof-type ridges, nanoscale ribs and windows of the T_FW were well maintained. The triangular roof-type ridges focus the light into the scale interior via multiple antireflections and form the HSAS. That structure is facilitates the capture of the light. Declining microribs run down the sides of the ridge that induces the internal light-scattering which assists in trapping light. Staggered windows are present between every two ridges. The windows elongate the light path length and enlarge the energy density distribution interspace, which implies a potentially important linkage with light-harvesting capacity. The ridges, microribs and windows construct the HSAS. After carbonizing the Ag_T_FW, the morphologies of the Ag@C_T_FW almost not change basically compared with the Ag_T_FW, and the HSAS was maintained well with effective light absorption performance. Further insight was gained regarding the morphologies and microstructures of the Ag@C_T_FW and the results are shown in Fig. 4(c) and (d). As shown in Fig. 4(c), Ag NPs deposited on the surface of the bio-template and agglomerated into a thin film. The inset of Fig. 4(c) is the SAED image displays ring and dot patterns, corresponding to the major and minor phases in the product respectively. The clear rings match well with the XRD results, and the relevant planes are indexed as (111), (200), (220) and (311), respectively. The lattice fringes with interplanar distance of $d_{Ag(111)}$=0.24 nm is exhibited in the HRTEM image (Fig. 4(d)).

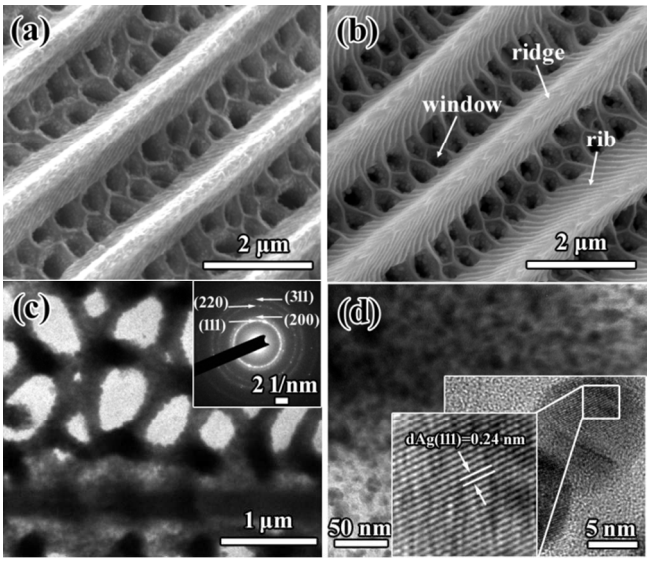

Fig. 4. FESEM images of (a) Ag_T_FW and (b) Ag@C_T_FW. (c)-(d) TEM images of Ag@C_T_FW. The inset of (c) is the SAED image of Ag@C_T_FW. The inset of (d) is the HRTEM image of Ag@C_T_FW.

To explain the mechanism of the enhanced IR absorption over a broadband wavelength region, we compared the absorption properties of the Ag@C_T_FW with Ag_T_FW, C_T_FW (the carbonized T_FW using the same carbonization process as the Ag@C_T_FW), T_FW and BlueTec eta plus_Cu over the wavelength range of 300-2500 nm (Fig. 5(a)) and 2.5-15μm (Fig. 5(b)). BlueTec eta plus_Cu is a commercial absorber that functions as a solar thermal collector. Capable of absorbing extremely high levels of sunlight, BlueTec eta plu_Cu effectively transforms solar energy into heat (BlueTec GmbH & Co KG, Hese Germany). As shown in Fig. 5(a), the T_FW shows an excellent absorption over the visible light region because of the coupling effect between the melanin/chitin composite and the HSAS of T_FW.[37, 38] Compared with the absorption properties of the T_FW, the C_T_FW provided an enhancement in absorption in the IR region, demonstrating that amorphous carbon provides better IR absorption than the melanin/chitin composite of T_FW. These results also induce that the enhanced infrared absorption property is not only decided by the super absorption structure, but also dictated by the absorption properties of materials. As shown in Fig. 5(a) and the inset of Fig. 5(a), the absorption spectra of Ag@C_T_FW and Ag_T_FW display the characteristic peak at 312 nm and 318 nm, respectively, resulted from the Ag NPs plasmon resonance.[39] Over the wavelength region of NIR (Fig. 5(a)) and mid infrared (MIR) (Fig. 5(b)), the Ag_T_FW exhibits a more intensive absorption, compared with C_T_FW and T_FW. The reason is that, firstly, the plasmon resonant of the Ag NPs resulted in an enhanced absorption. Secondly, the coherent coupling between adjacent resonant systems created an enhancement of light absorption over a broadband IR region.[22, 40] Furthermore, the plasmon resonant and the coherent coupling between adjacent resonant systems integrate with the HSAS of T_FW which can create the broadband light absorption enhancement with a more intensity. Remarkably, the Ag@C_T_FW possesses a more effective broadband light absorption, compared with Ag_T_FW, because the carbon matrix is better for infrared absorption compared with the melanin/chitin composite matrix. Consequently, the Ag@C_T_FW coupled the plasmonic resonances to carbon-matrix HSAS. By optimizing the coupling among the plasmon, functional structure and the matrix materials, the samples can possess a further enhanced broadband light absorption property. Moreover, the intensive absorption enhancement was achieved over the wavelength range of 2.5-15 μm (Fig. 5(b)). Compared with the BlueTec eta plus_Cu, the average absorbance intensities of the Ag@C_T_FW increased by 42.75% in the wavelength range of 300-2500 nm, and was as much as 28.7 times greater in the wavelength range of 2.5-15 μm.

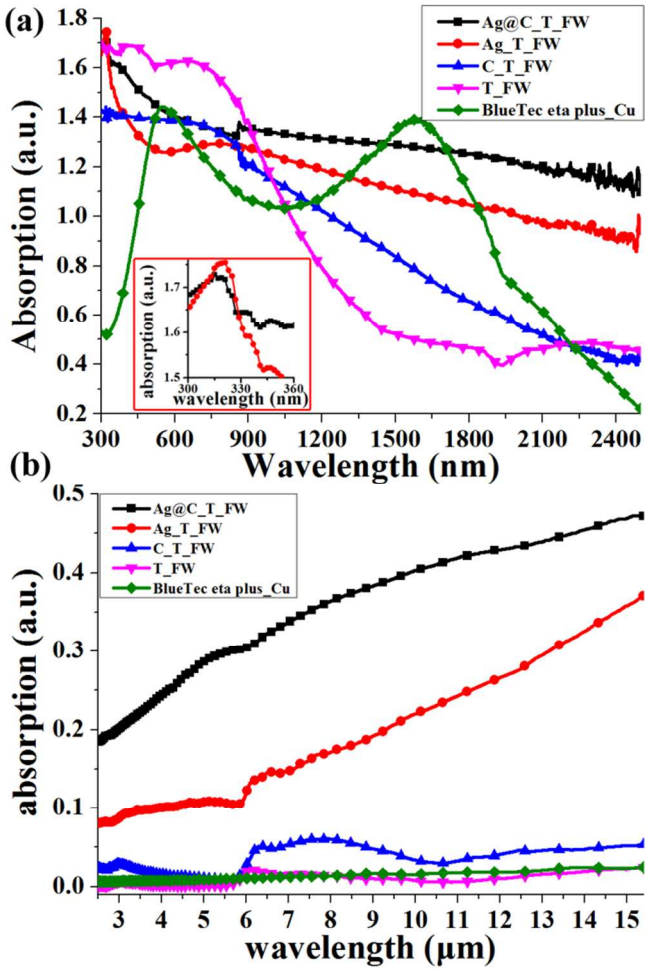

Fig. 5. Absorption spectra of Ag@C_T_FW, Ag_T_FW, C_T_FW, T_FW and BlueTec eta plus_Cu, (a) over the wavelength range of 300-2500 nm, (b) over the wavelength range of 2.5-15 μm. The inset of Fig. 5(a) is the absorption spectra of Ag@C_T_FW and Ag_T_FW over the wavelength range of 300-360 nm with a higher magnification.

To further demonstrate that the plasmon resonant and the coherent coupling between adjacent resonant systems create and enhancement in absorption over a broadband IR region, the FDTD simulation was used. From Fig. 6(a) and (a1), we can find that Ag nanospheres array when the Ag nanospheres touched each other exhibits multiple absorbance maxima over the wavelength range of 300-600 nm. While increasing the separation distance of the Ag nanospheres, the multiple absorbance maxima became weaker gradually and finally disappeared. The absorption spectra exhibited only a single peak when the separation distance increased to 40 nm which effectively considered as single particles. The first peak, located near the resonance peak of single particles, is attributed to the quadrupole plasmon excitation in the coupled Ag nanosperes, while the other peaks at longer wavelength are attributed to the dipole plason resonance of the Ag nanospheres.[41] The multiple absorbance maxima is attributed the coupling effect of plasmon response of the Ag nanospheres.[31, 41, 42] The oscillating electrons in one Ag nanosphere feel the electric field due to the oscillations in the adjacent Ag nanospheres, which can lead to a collective plasmon oscillation of the aggregated system.[41] As shown in Fig. 6(a) and (a2), the linked Ag nanospheres array exhibits a more enhanced broadband IR absorption performance compared with the other Ag nanospheres array when the Ag nanospheres are in different spacing. Moreover, the absorptions are decreased with gradually increasing the spacing d of the Ag nanospheres. When added the Ag nanospheres array to the surface of chitin, the Ag_chitin possesses the similar enhancement absorption performance over a broadband IR region and the absorption intensity is decreased when increase the spacing d of the Ag nanospheres. Consequently, the simulation results as shown in Fig. 6(a) and (b) indicate that the coherent coupling between adjacent resonant systems resulted in an enhanced IR absorption over a broadband wavelength region.[22] Furthermore, coherent coupling between adjacent resonant systems is demonstrated by the maps of the energy flux density amplitude. As shown in Fig. 6(c)-(f), the Ag nanospheres efficiently generated plasmons and substantially enhanced the electromagnetic field in the adjacent region between two nanospheres, providing hotspots especially located in the interparticle region.

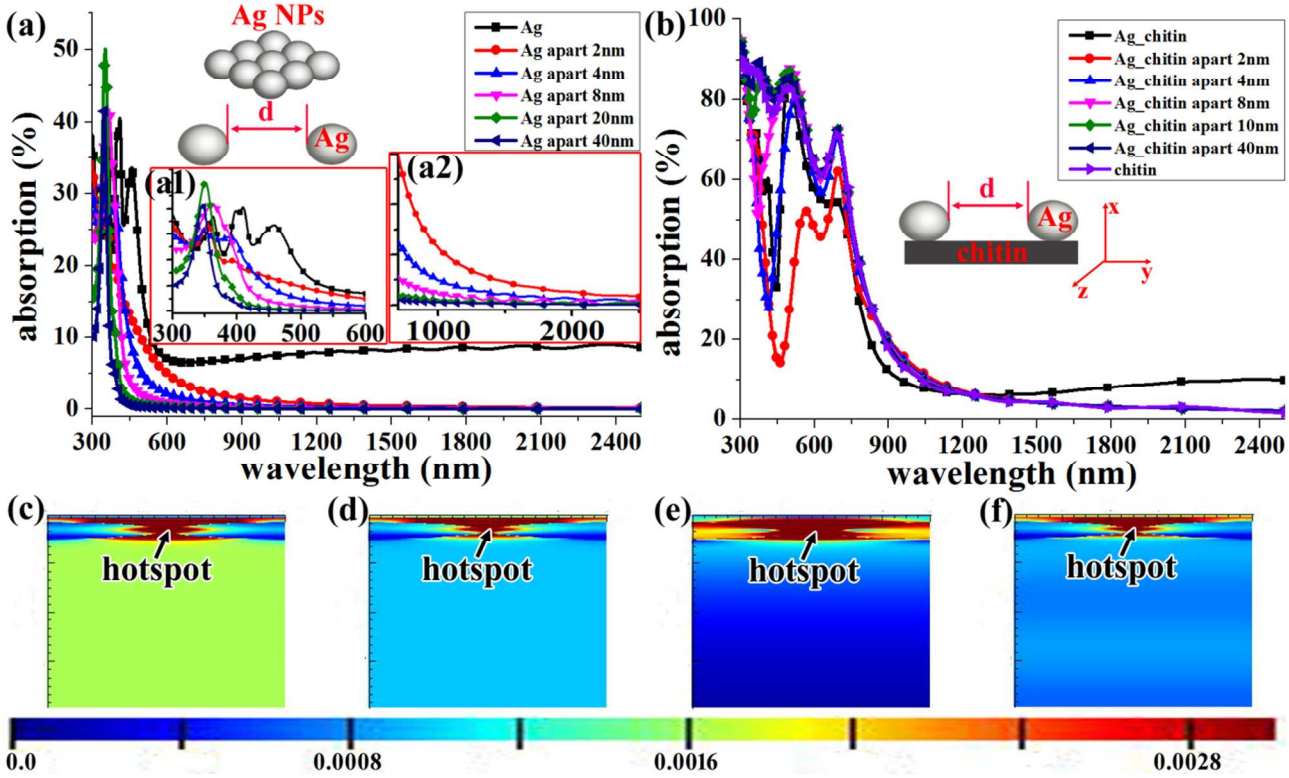

Fig. 6. FDTD simulation results for Ag nanospheres array (Ag) and added the Ag nanospheres array to the surface of chitin (Ag_chitin). (a) The absorption spectra of the Ag with the different spacing d=0 nm (Ag), d=2 nm (Ag apart 2nm), d=4 nm (Ag apart 4nm), d=8 nm (Ag apart 8nm), d=20 nm (Ag apart 20nm) and d=40 nm (Ag apart 40nm). (a1) and (a2) is the absorption spectra in the wavelength range of 300-600 nm and 700-2500 nm with a higher magnification, respectively. (b) The absorption spectra of chitin (chitin sheet) and the Ag_chitin with the different spacing d=0 nm (Ag_chitin), d=2 nm (Ag_chitin apart 2nm), d=4 nm (Ag_chitin apart 4nm), d=8 nm (Ag_chitin apart 8nm), d=20 nm (Ag_chitin apart 20nm) and d=40 nm (Ag_chitin apart 40nm). (c) and (d) Maps of the energy flux density amplitude of Ag, in which the incident light is 470 nm and 980 nm, respectively; (e) and (f) Maps of the energy flux density amplitude of Ag_chitin, in which the incident light is 470 nm and 980 nm, respectively.

To better demonstrate the plasmon resonant and the coherent coupling between adjacent resonant systems integrated with the HSAS of T_FW which can create the broadband light absorption enhancement with a more intensity over the IR region, we used the FDTD to calculate the absorption properties of the Ag_chitin, Ag_T_FW and T_FW (Fig. 7). Compared with the absorption spectra of T_FW, that of Ag_T_FW exhibits an enhancement in absorption over a broadband IR region. Moreover, the absorption intensity of Ag_T_FW integrated from 300 nm to 2500 nm exhibits about 1.3 times enhancement compared with absorption intensity of absorption intensity of T_FW. These finding indicate that the plasmon resonant add the coherent coupling between adjacent resonant systems can enhance IR absorption over a broadband. Following, by compared with the absorption spectra of Ag_chitin, that of Ag_T_FW exhibits a more intensive absorption over the wavelength range over 300-2500 nm, which demonstrates that the plasmon integrate with the HSAS can achieve an enhanced broadband light absorption. The absorption intensity of Ag_T_FW (with HSAS) integrated from 300 nm to 2500 nm exhibits about 4.05 times enhancement compared with absorption intensity of absorption intensity of Ag_chitin (without HSAS). Furthermore, compared with the optical absorption of HCP Au nanoshell[22] (without HSAS), the Ag_T_FW possesses a more intensive optical absorption capability. Consequently, the Ag_T_FW achieved that the plasmon resonant and the coherent coupling between adjacent resonant systems integrate with the HSAS, created the broadband light absorption enhancement with a more intensity, specially, over the IR region. And the simulation results that the Ag_T_FW exhibited an enhancement broadband IR absorption are in excellent agreement with those experimentally observed as shown in Fig. 5(a) and Fig. 7. However, the observed different in the absorption spectra in the visible light region can be attributed to only a monolayer Ag nanospheres covered on the surface of the HSAS for the FDTD simulation model which generated a lower reflection resulted from monolayer Ag layer. Indeed, for the experimental sample, the multilayer Ag nanospheres covered on the surface of the HSAS of the T_FW which generated a higher reflection compared with the FDTD simulation model.

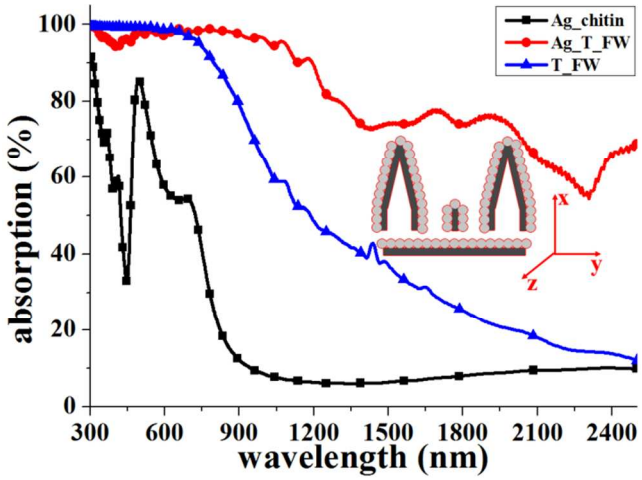

Fig. 7. FDTD calculations for the absorption spectra of Ag_chitin, Ag_T_FW and T_FW.

The plasmon resonant and the coherent coupling between adjacent resonant systems integrated with the HSAS is further demonstrated by the maps of the energy flux density amplitude of T_FW and Ag_T_FW, as shown in Fig. 8. The intensive energy density distributed on the region where is located in the windows and between the two ridges. These finding demonstrate that the triangular roof type ridges possess a facilitating light capturing capacity because of the antireflection performance of the triangular roof type structure. Interestingly, the obvious hotspots situate on the surface of the Ag nanospheres layer which resulted from the plasmon resonant and the coherent coupling between adjacent resonant systems (Fig. 8(c) and (d)). From the energy flux density distribution maps of Ag_T_FW, we can come to the conclusion that the Ag_T_FW and Ag@C_T_FW achieved that the plasmon resonant and the coherent coupling between adjacent resonant systems integrate with the HSAS.

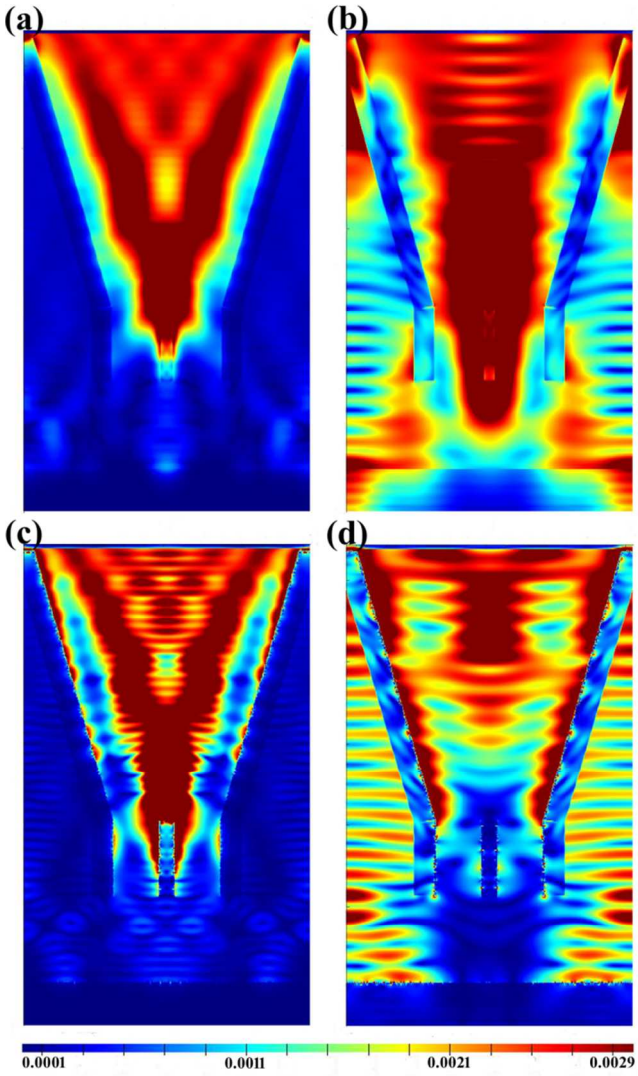

Fig. 8. (a) and (b) Maps of the energy flux density amplitude of T_FW, in which the incident light is 470 nm and 980 nm, respectively; (c) and (d) Maps of the energy flux density amplitude of Ag_T_FW, in which the incident light is 470 nm and 980 nm, respectively.

In order to optimise the enhancement of the broadband light absorption, the parametric study is carried out taking into account the size of Ag NPs which integrated with the HSAS of T_FW. By compared with the absorption spectra of Ag_T_FW with different Ag NPs diameter (20nm, 40nm 60nm and 80nm), we can find that the intensity of the light absorption is decreased with increasing the diameter of the Ag NPs, except for the wavelength range located near the 1600 nm. (Fig. 9(a) and (b)) However, compared with the absorption spectra of Ag_T_FW with the Ag NPs diameter equalled 20 nm, the enhancement of the light absorption of Ag_T_FW with the Ag NPs diameter equalled 10 nm is not significant, especially over the wavelength range located near the 838 nm and 1600 nm. As shown in Fig. 9(b), the absorption is more effective over the purple rectangle region which demonstrated that the Ag_T_FW with the Ag NPs diameter equalled from 12 to 15 nm possesses more effective light absorption. Consequently, the Ag NPs with suitable size integrated with the HSAS of T_FW can possess more effective light absorption over a broadband range. These simulation results offer a guidance for our further experiment to

obtain a more effective light absorption material by controlling the diameter of Ag NPs of the Ag_T_FW and Ag@C_T_FW with a suitable size.

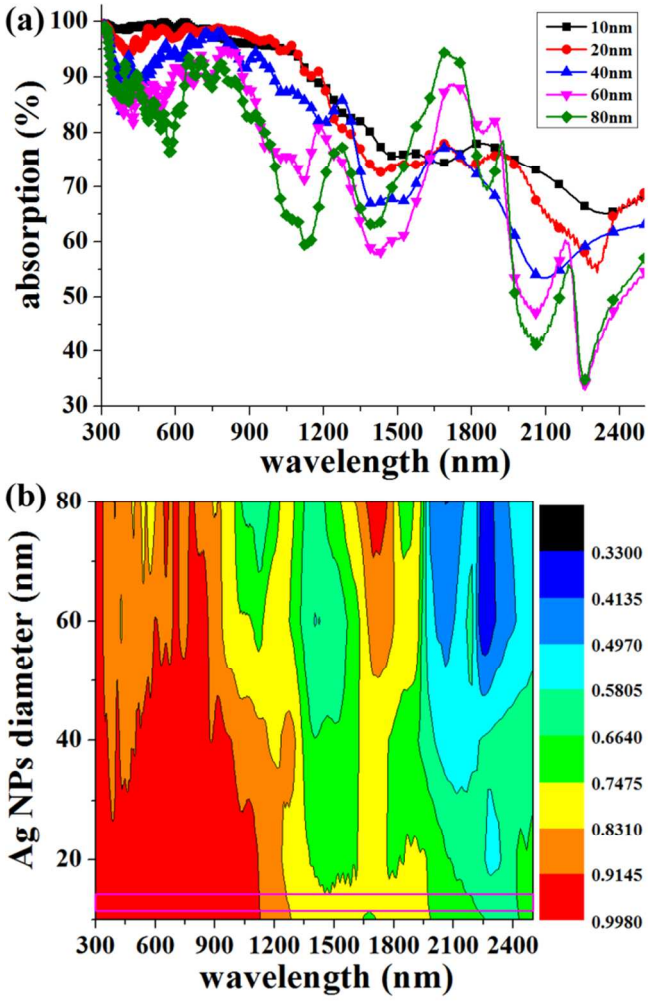

Fig. 9. (a) FDTD calculations for the absorption spectra of Ag_T_FW with different Ag NPs diameter (10nm, 20nm, 40nm 60nm and 80nm), respectively. (b) The simulation of the absorption spectra of Ag_T_FW versus Ag NPs diameter.

Conclusions

In this work, we combined chemosynthesis and biomimetic techniques using the T_FW as the biomimetic-template to fabricate the Ag@C_T_FW with a HSAS without the requirement of expensive equipment and energy intensive processes. The Ag@C_T_FW coupled the plasmonic resonances to carbon-based HSAS and achieved a drastically enhanced infrared absorption over a broad spectral range, specially, over the NIR region. However, the enhancement absorption was also obtained in the MIR range. We find that the IR absorption is closely related to the HSAS and the SPR of the Ag nanoparticles. Using the FDTD method, the distribution of the intensive energy density near the Ag NPs surface and the absorption spectra were simulated. Based on the experiment and simulation results, the improvement can be explained that, firstly, the plasmon resonant of the Ag NPs resulted in an enhanced absorption. Secondly, the coherent coupling between adjacent resonant systems created the broadband light absorption enhancement. Furthermore, the plasmon resonant and the coherent coupling between adjacent resonant systems integrate with the HSAS of T_FW which can create the broadband light absorption enhancement with a more intensity. Consequently, the Ag@C_T_FW provides a new perspective for coupling the plasmon and the coherent coupling between adjacent resonant systems with HSAS. The work successfully provides a new route to enhance broadband infrared absorption and utilize the solar energy in infrared range at lower cost. And appear to be useful in applications of plasmon for optoelectronics, photovoltaics, photothermal and related technologies.

Acknowledgements

This work was supported by the National Natural Science Foundation of China (no. 51202145, no. 51131004 and no. 51171110), the National Basic Research Program of China (973 Program, no. 2011cb922200) and Research Fund for the Doctoral Program of Higher Education of China (20120073120006 and 20120073130001).

Notes and references

State Key Laboratory of Metal Matrix Composites, Shanghai Jiao Tong University, 800 Dongchuan Road, Shanghai, 200240, P. R. China. E-mail: wangzhang@sjtu.edu.cn; zhangdi@sjtu.edu.cn; Fax: +86-21-34202749; Tel: +86-21-34202634

1. A. Dmitriev, T. Pakizeh, M. Käll and D. S. Sutherland, *Small*, 2007, **3**, 294-299.
2. J. Zhang, Y. Fu, M. H. Chowdhury and J. R. Lakowicz, *Nano letters*, 2007, **7**, 2101-2107.
3. R. Gordon, D. Sinton, K. L. Kavanagh and A. G. Brolo, *Acc. Chem. Res.*, 2008, **41**, 1049-1057.
4. I. A. Larmour and D. Graham, *Analyst*, 2011, **136**, 3831-3853.
5. B. Ng, J. Wu, S. M. Hanham, A. I. Fernández‐Domínguez, N. Klein, Y. F. Liew, M. B. Breese, M. Hong and S. A. Maier, *Adv. Optical Mater.*, 2013, **1**, 543-548.
6. A. M. Gobin, M. H. Lee, N. J. Halas, W. D. James, R. A. Drezek and J. L. West, *Nano letters*, 2007, **7**, 1929-1934.
7. E. M. Larsson, C. Langhammer, I. Zorić and B. Kasemo, *Science*, 2009, **326**, 1091-1094.
8. M. A. Mackey, M. R. Ali, L. A. Austin, R. D. Near and M. A. El-Sayed, *J. Phys. Chem B*, 2014, **118**, 1319-1326.
9. Y. Ma, X. Liang, S. Tong, G. Bao, Q. Ren and Z. Dai, *Adv. Funct. Mater.*, 2013, **23**, 815-822.
10. S. T. Sivapalan, B. M. DeVetter, T. K. Yang, T. van Dijk, M. V. Schulmerich, P. S. Carney, R. Bhargava and C. J. Murphy, *ACS Nano*, 2013, **7**, 2099-2105.
11. Y. Tan, J. Gu, L. Xu, X. Zang, D. Liu, W. Zhang, Q. Liu, S. Zhu, H. Su and C. Feng, *Adv. Funct. Mater.*, 2012, **22**, 1578-1585.
12. Y. Tan, J. Gu, X. Zang, W. Xu, K. Shi, L. Xu and D. Zhang, *Angew. Chem. Int. Ed.*, 2011, **123**, 8457-8461.
13. C. H. Moran, M. Rycenga, X. Xia, C. M. Cobley and Y. Xia, *Nanotechnology*, 2014, **25**, 014007.

14. X. Chen, B. Jia, J. K. Saha, B. Cai, N. Stokes, Q. Qiao, Y. Wang, Z. Shi and M. Gu, *Nano letters*, 2012, **12**, 2187-2192.
15. H. Tan, R. Santbergen, A. H. Smets and M. Zeman, *Nano letters*, 2012, **12**, 4070-4076.
16. H. A. Atwater and A. Polman, *Nat. mater.*, 2010, **9**, 205-213.
17. V. E. Ferry, J. N. Munday and H. A. Atwater, *Adv. Mater.*, 2010, **22**, 4794-4808.
18. T. Jensen, R. Van Duyne, S. Johnson and V. Maroni, *Applied Spectroscopy*, 2000, **54**, 371-377.
19. J. Kundu, F. Le, P. Nordlander and N. J. Halas, *Chem. Phys. Lett.*, 2008, **452**, 115-119.
20. K. Ataka, F. Giess, W. Knoll, R. Naumann, S. Haber-Pohlmeier, B. Richter and J. Heberle, *J. Am. Chem. Soc.*, 2004, **126**, 16199-16206.
21. C.-W. Cheng, M. N. Abbas, C.-W. Chiu, K.-T. Lai, M.-H. Shih and Y.-C. Chang, *Opt. Express*, 2012, **20**, 10376-10381.
22. F. Le, D. W. Brandl, Y. A. Urzhumov, H. Wang, J. Kundu, N. J. Halas, J. Aizpurua and P. Nordlander, *ACS Nano*, 2008, **2**, 707-718.
23. T. Wang, V. H. Nguyen, A. Buchenauer, U. Schnakenberg and T. Taubner, *Opt. Express*, 2013, **21**, 9005-9010.
24. J. n. M. Hoffmann, X. Yin, J. Richter, A. Hartung, T. W. Maß and T. Taubner, *J. Phys. Chem. C*, 2013, **117**, 11311-11316.
25. L. V. Brown, K. Zhao, N. King, H. Sobhani, P. Nordlander and N. J. Halas, *J. Am. Chem. Soc.*, 2013, **135**, 3688-3695.
26. H. Wang, D. W. Brandl, P. Nordlander and N. J. Halas, *Acc. Chem. Res.*, 2007, **40**, 53-62.
27. S. E. Skrabalak, J. Chen, Y. Sun, X. Lu, L. Au, C. M. Cobley and Y. Xia, *Acc. Chem. Res.*, 2008, **41**, 1587-1595.
28. X. Huang, S. Neretina and M. A. El‐Sayed, *Adv. Mater.*, 2009, **21**, 4880-4910.
29. D. Chanda, K. Shigeta, T. Truong, E. Lui, A. Mihi, M. Schulmerich, P. V. Braun, R. Bhargava and J. A. Rogers, *Nat. commun.*, 2011, **2**, 479.
30. T. Jägeler-Hoheisel, J. Cordeiro, O. Lecarme, A. Cuche, C. Girard, E. Dujardin, D. Peyrade and A. Arbouet, *J. Phys. Chem. C*, 2013, **117**, 23126-23132.
31. A. S. Urban, X. Shen, Y. Wang, N. Large, H. Wang, M. W. Knight, P. Nordlander, H. Chen and N. J. Halas, *Nano letters*, 2013, **13**, 4399-4403.
32. J. Li, M. Hossain, B. Jia, D. Buso and M. Gu, *Opt. Express*, 2010, **18**, 4491-4498.
33. X. Huang, S. Tang, B. Liu, B. Ren and N. Zheng, *Adv. Mater.*, 2011, **23**, 3420-3425.
34. W. Shi, H. Zeng, Y. Sahoo, T. Y. Ohulchanskyy, Y. Ding, Z. L. Wang, M. Swihart and P. N. Prasad, *Nano Lett.*, 2006, **6**, 875-881.
35. Y. Kang, X. Ye and C. B. Murray, *Angew. Chem. Int. Ed.*, 2010, **49**, 6156-6159.
36. L. Cheng, C. Ma, G. Yang, H. You and J. Fang, *J. Mater. Chem. A*, 2014, **2**, 4534-4542.
37. Q. Zhao, X. Guo, T. Fan, J. Ding, D. Zhang and Q. Guo, *Soft Matter*, 2011, **7**, 11433-11439.
38. A. Herman, C. Vandenbem, O. Deparis, P. Simonis and J. P. Vigneron, *Proc. of SPIE*, 2011, **8094**, 80940H1-12.
39. G. S. Métraux and C. A. Mirkin, *Adv. Mater.*, 2005, **17**, 412-415.
40. Z. Ye, S. Chaudhary, P. Kuang and K.-M. Ho, *Opt. Express*, 2012, **20**, 12213-12221.
41. S. K. Ghosh and T. Pal, *Chem. Rev.*, 2007, **107**, 4797-4862.
42. E. Prodan, C. Radloff, N. Halas and P. Nordlander, *Science*, 2003, **302**, 419-422.